

RESEARCH

Open Access



# Biodegradable and biocompatible subcutaneous implants consisted of pH-sensitive mebendazole-loaded/folic acid-targeted chitosan nanoparticles for murine triple-negative breast cancer treatment

Amirhosein Kefayat<sup>1,4</sup>, Maryam Hosseini<sup>2</sup>, Fatemeh Ghahremani<sup>3</sup>, Nafise Arbab Jolfaie<sup>4</sup> and Mohammad Rafienia<sup>4\*</sup>

## Abstract

**Background:** Mebendazole (MBZ) is a well-known anti-parasite drug with significant anti-cancer properties. However, MBZ exhibits low solubility, limited absorption efficacy, extensive first-pass effect, and low bioavailability. Therefore, multiple oral administration of high dose MBZ is required daily for achieving the therapeutic serum level which can cause severe side effects and patients' non-compliance.

**Method:** In the present study, MBZ-loaded/folic acid-targeted chitosan nanoparticles (CS-FA-MBZ) were synthesized, characterized, and used to form cylindrical subcutaneous implants for 4T1 triple-negative breast tumor (TNBC) treatment in BALB/c mice. The therapeutic efficacy of the CS-FA-MBZ implants was investigated after subcutaneous implantation in comparison with Control, MBZ (40 mg/kg, oral administration, twice a week for 2 weeks), and CS-FA implants, according to 4T1 tumors' growth progression, metastasis, and tumor-bearing mice survival time. Also, their biocompatibility was evaluated by blood biochemical analyzes and histopathological investigation of vital organs.

**Results:** The CS-FA-MBZ implants were completely degraded 15 days after implantation and caused about 73.3%, 49.2%, 57.4% decrease in the mean tumors' volume in comparison with the Control ( $1050.5 \pm 120.7 \text{ mm}^3$ ), MBZ ( $552.4 \pm 76.1 \text{ mm}^3$ ), and CS-FA ( $658.3 \pm 88.1 \text{ mm}^3$ ) groups, respectively. Average liver metastatic colonies' number per microscope field at the CS-FA-MBZ group ( $2.3 \pm 0.7$ ) was significantly ( $P < 0.05$ ) lower than the Control ( $9.6 \pm 1.7$ ), MBZ ( $5.0 \pm 1.5$ ), and CS-FA ( $5.2 \pm 1$ ) groups. In addition, the CS-FA-MBZ treated mice exhibited about 52.1%, 27.3%, and 17% more survival days after the cancer cells injection in comparison with the Control, MBZ, and CS-FA groups, respectively. Moreover, the CS-FA-MBZ implants were completely biocompatible based on histopathology and blood biochemical analyzes.

**Conclusion:** Taking together, CS-FA-MBZ implants were completely biodegradable and biocompatible with high therapeutic efficacy in a murine TNBC model.

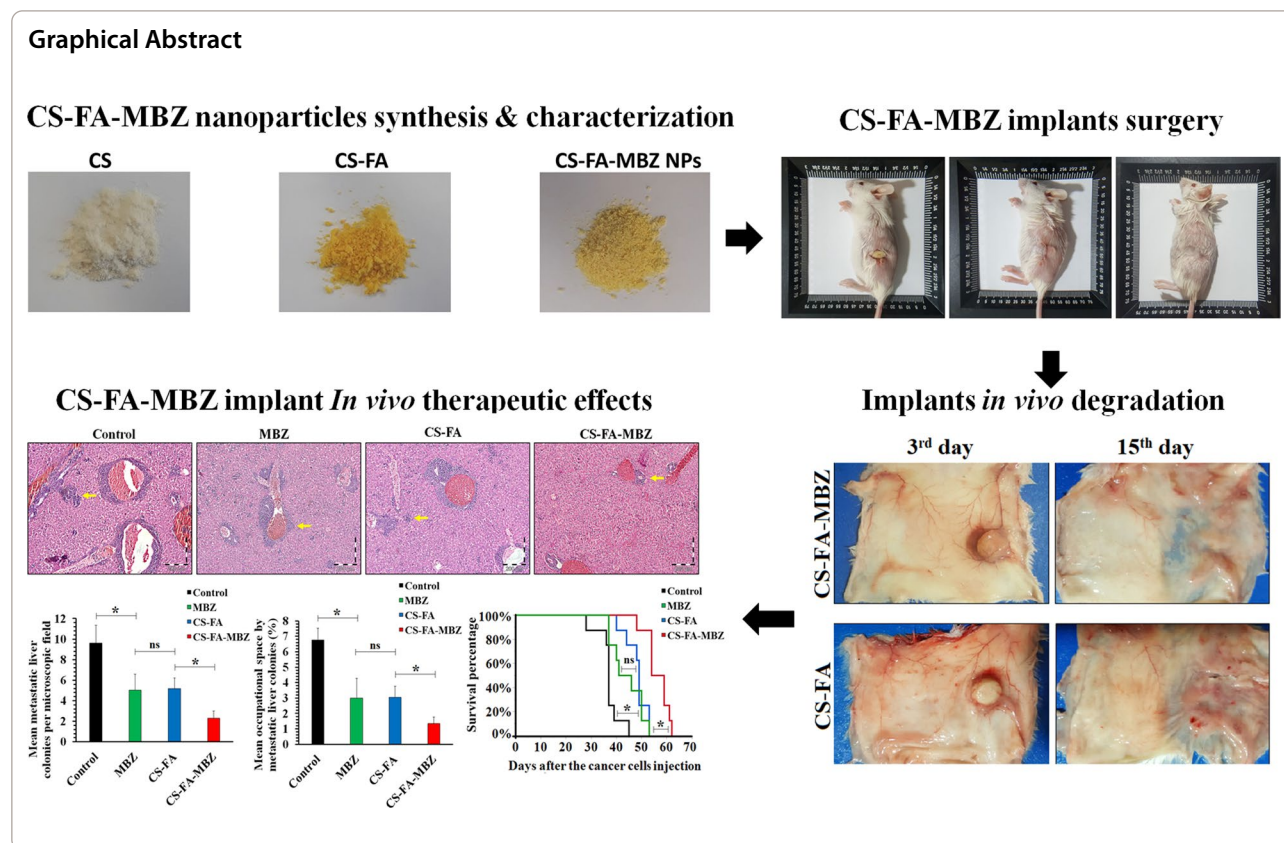
**Keywords:** Mebendazole, Chitosan nanoparticles, Subcutaneous implants, Folic acid, Triple-negative breast cancer

\*Correspondence: m\_rafienia@med.mui.ac.ir

<sup>4</sup> Biosensor Research Center, Isfahan University of Medical Sciences, Isfahan, Iran

Full list of author information is available at the end of the article





## Background

Breast cancer is the most common malignancy among women and the leading cause of cancer-related deaths in the female gender [1]. About 20% of all diagnosed breast cancers are categorized as triple-negative breast cancer (TNBC). This acronym simply means that the tumor doesn't express estrogen, progesterone, and human epidermal growth factor-2 receptors on its cells' surface [2]. TNBC is significantly more aggressive and invasive than other subtypes of breast cancer and exhibits higher relapse rates and shorter recurrence period [3]. Therefore, due to the absence of well-defined molecular targets, currently, the only therapeutic approach for TNBC patients is chemotherapy [4, 5]. However, the outcome of chemotherapy with currently approved drugs isn't satisfying, and poor therapeutic response, severe side effects, and development of multidrug resistance are still big challenges in TNBC chemotherapy [6, 7].

Mebendazole (MBZ) is a well-known antihelminthic drug, with high biocompatibility and low price which has been repurposed for anti-neoplastic treatment [8]. Many studies have reported anti-proliferative, pro-apoptotic, and anti-metastatic effects of MBZ on different cancer cell lines including chemoresistant cancer cell lines [9, 10]. MBZ treatment causes a decrease or complete arrest

of tumor growth, significant inhibition of tumor metastasis, and an increase of tumor-bearing mice survival time in different animal models of cancer [11–16]. Anti-neoplastic activities of MBZ can be attributed to inhibition of tubulin polymerization, decrease of tumor angiogenesis, blocking of pro-survival pathways, inhibition of matrix metalloproteinases function, and multi-drug resistance protein transporters activity [8, 17–19]. However, MBZ has limited bioavailability after oral administration as only 20% of the dosage reaches the systemic circulation. This can be related to the low solubility of MBZ, limited absorption efficacy, and extensive first-pass effect following oral administration [20, 21]. Therefore, a high dose of MBZ is required for achieving the therapeutic serum level which can cause severe adverse effects and patients' non-compliance [22].

Drug-releasing implants have gained lots of attention for controlled drug release in long-term treatments, especially cancer chemotherapy [23, 24]. Implants that contain chemotherapy drugs have exhibited many advantages over intravenous or oral drug administration routes including the elimination of daily multiple injections and maintenance of the steady-state concentration of the drug [25–29]. Biodegradable polymers are the most utilized materials for developing these implants [30].

Chitosan (CS) is a well-known biodegradable biopolyaminosaccharide with a natural origin. The chitosan-based drug carriers and implants exhibit high biodegradability, low toxicity, and appropriate biocompatibility. In addition, chitosan per se has considerable anti-proliferative, pro-apoptotic, anti-angiogenic, and anti-metastatic effects on different types of tumors [31–33]. Different forms of chitosan-based drug delivery systems have been used and chitosan nanoparticles are one of the most advanced ones for the enhancement of anti-cancer drugs efficacy. They can be defined as spherical, biocompatible, and biodegradable nanostructures with high drug-loading efficacy [34–36]. Chitosan nanoparticles can be used for the controlled release of different types of drugs and enhancement of tumor drug delivery efficacy [37–41]. In addition, chitosan nanoparticles decorating with targeting ligands that can bind to the malignant cells' surface receptors have received lots of attention for enhancement of tumor drug delivery efficacy [42, 43]. One of the most efficient targeting agents for cancer cells specific targeting is folic acid (FA) due to overexpression of the folate receptor on their membrane in comparison with normal cells. Furthermore, FA has the potential to conjugate directly to polymeric nanoparticles (e.g., through click chemistry), leading to fabrication of novel targeted drug carriers for an efficient delivery [44]. FA has many advantages over other targeting agents, including low molecular weight, simple chemical properties, receptor-mediated endocytosis of the folic acid-decorated carriers, extremely low immunogenicity, overexpression on cancer cells membrane, and limited expression on normal cells' surface [45–48]. In this regard, many different studies have used FA to decorate their nanostructures for cancer cells targeting and tumor-specific drug release in different cancer models [47, 49]. It should be mentioned that although TNBC cells are known due to the lack of different molecular targets on their membrane, FA is a highly overexpressed receptor on their surface [50–52]. Therefore, FA-modified drug delivery systems can increase the drug concentration at the TNBC tumors site and decline its side effects at normal tissues [53].

In the present study, MBZ-loaded/folic acid-targeted chitosan nanoparticles (CS-FA-MBZ) were used to form cylindrical implants for 4T1 triple-negative breast tumor treatment in BALB/c mice. The therapeutic efficacy of the CS-FA-MBZ implants was investigated after subcutaneous implantation in comparison with Control, MBZ, and CS-FA implants according to 4T1 tumors' growth progression, metastasis, and tumor-bearing mice survival time. Also, the CS-FA-MBZ implant's biocompatibility was evaluated by blood biochemical analyzes and vital organs histopathological investigations. In this study, 4T1 murine triple-negative mammary carcinoma was used

as an experimental animal model with high similarity to human TNBC. This cell line is a highly tumorigenic and invasive cancer cell line that can spontaneously metastasize from the primary tumor in the mammary gland to multiple distant sites. Also, its metastasis pattern is very similar to that of human breast cancer [54–57]. Although CS-FA nanoparticles have been studied previously as a drug delivery carrier, according to the best of our knowledge, this is the first study to load MBZ in the CS-FA to form CS-FA-MBZ for cancer treatment. In addition, we put on step beyond and designed completely biodegradable scaffolds using the CS-FA-MBZ nanoparticles which by their degradation in the host subcutaneous space, their ingredients (FA-CS-MBZ nanoparticles) will reach the blood circulation for causing their anti-cancer therapeutic effects without any remaining residues at the site of implantation. It should be mentioned that most of the previously studied drug-releasing implants have been implanted at the tumor site or its resected location to prevent its local recurrence [58–60]. However, considerable percentage of cancer patients (including breast cancer patients) experience further metastasis in the distant organs and it is apparent that local release of drug in the tumor site from these scaffolds is not effective for them at all. In addition, some cancer patients are suffering from diffuse metastatic colonies or even unresectable tumor which applying the previously reported drug-releasing scaffolds in the inner of these lesions is practically impossible.

## Materials and methods

### Material

Medium-molecular weight chitosan (190–310 kDa, MMW), Sodium tripolyphosphate (TPP), 1-ethyl-3-(3-dimethylaminopropyl) carbodiimide (EDC), N-hydroxysuccinimide (NHS), folic acid (97%, FA), Tween-80 (a non-ionic surfactant), mebendazole (MBZ), ammonia (25%, NH<sub>4</sub>OH), acetic acid, dimethyl sulfoxide (DMSO), phosphate-buffered saline powder (pH = 7.4 PBS), methanol and acetone were purchased from Sigma-Aldrich (Germany) and used without further purification unless stated otherwise. RPMI 1640, fetal bovine serum (FBS), MTT (3-(4,5-dimethylthiazol-2-yl)-2,5-diphenyltetrazolium bromide), phosphate buffer saline (PBS), penicillin/streptomycin, ethanol (96%, v/v), trypsin–EDTA (0.25%) were purchased from Merck (Germany).

### Conjugation of folic acid to chitosan (CS-FA preparation)

CS-FA was fabricated as reported in the literature [61]. Briefly, 0.5 g of FA and 0.2 g of EDC were initially dissolved in anhydrous DMSO (20 mL) under constant stirring at room temperature (2 h). Then, the solution was dropped into the CS solution 0.5% (w/v) prepared in

acetate buffer (0.1 M, pH 4.7) and at room temperature in dark for 16 h. Thereafter, the pH of the solution was adjusted to 9.0 by the addition of NaOH (1.0 M). The resulting precipitate was collected by centrifugation, then purified by dialysis against phosphate-buffered saline (PBS, pH 7.4) for 2 days and against water for another 4 days. Finally, yellow-colored CS-FA products were collected and freeze-dried.

#### Preparation of the CS-FA-MBZ nanoparticles

CS-FA-MBZ nanoparticles were synthesized according to the previously reported method with some modifications [62]. Initially, CS-FA (0.1 g) was dissolved in a solution containing acetic acid (1% v/v, 20 mL), then left under stirring at room temperature in dark for 16 h to prepare a solution of CS-FA (0.5% w/v). The pH of the solution was adjusted to 4.8 by the addition of NaOH (1.0 M). Afterward, 250  $\mu$ L of Tween-80 was added dropwise and left for 2 h under stirring at 45 °C. In the next step, 0.01 g MBZ was dissolved in 0.5 M methanolic hydrochloride [63] and then added to the former solution and stirred for 30 min. Finally, 10 mL TPP aqueous solution (0.5% w/v) was dropped to the CS-FA solution slowly under magnetic stirring (800 rpm) at room temperature for 1 h then the nanoparticles were collected by centrifugation (12,000 rpm, 30 min). The resulting CS-FA-MBZ nanoparticles were lyophilized and stored.

#### Calculation of MBZ loading

MBZ was loaded during the formation of CS-FA nanoparticles as reported in the literature [62]. To calculate MBZ encapsulation efficacy (EE%) and loading capacity (LC%), unloaded MBZ content in the supernatant of the last step was determined through a calibration curve of MBZ standard solution by UV–Visible spectroscopy at 234 nm [63]. The MBZ loading ratio of the nanoparticles was calculated by the following Eqs. (1 and 2):

$$\text{MBZ encapsulation efficacy (EE\%)} = \frac{\text{Mass of the loaded MBZ}}{\text{Mass of the initial MBZ}} \times 100 \quad (1)$$

$$\text{MBZ loading capacity (LC\%)} = \frac{\text{Mass of the loaded MBZ}}{\text{Mass of the final product}} \times 100 \quad (2)$$

#### In vitro drug release pattern of the CS-FA-MBZ nanoparticles

To evaluate the release behavior of MBZ from CS-FA-MBZ nanoparticles, 5 mg of the CS-FA-MBZ nanoparticles were immersed in PBS solution containing Tween-80 (0.1% w/v) at pH values of 2.2, 5.5, 6.8, and 7.4 at 37 °C in dark under shaking at 100 rpm. The released MBZ

was assessed at 0.5 h, 1 h, 2 h, 4 h, 6 h, 8 h, 1 day, 2 days, 3 days, 5 days, and 7 days time points after immersing the nanoparticles in PBS [64]. At each predetermined time point, the nanoparticles were centrifuged (10,000 rpm for 15 min) and the released medium was collected and replaced with equivalent fresh PBS solution. The cumulative percentage of released MBZ was determined by UV–Visible spectrophotometry at 234 nm.

#### Nanoparticle's characterization and implants fabrication

To assess the structure and interaction of CS, CS-FA, and CS-FA-MBZ, Fourier Transform Infrared Spectroscopy (FTIR) was used by a Bruker Equinox 55 spectrometer with the KBr pellets method. To evaluate the size and morphology of nanoparticles, scanning electron microscopy (SEM; FEI ESEM QUANTA 200, MIRAI and MIRAI Tescan) and transmission electron microscopy (TEM; Philips RM-208, operating voltage: 100 kV) images were acquired. The average size and size distribution of particles were determined by measuring the diameter of 100 particles of SEM images using ImageJ software. The ultraviolet–visible (UV–vis) spectra were recorded by a PerkinElmer Lambda 950 spectrophotometer (wavelength range: 200–800 nm). <sup>1</sup>H-NMR experiment was recorded on Avance III ultrasield spectrometer manufactured by Bruker at a field strength of 11.7 T (500 MHz) and the corresponding data was collected using MestReNova software. The zeta potential, hydrodynamic size distribution, and polydispersity of the prepared nanoparticles were measured by Dynamic Light Scattering (DLS) (Malvern Instruments). A well-dispersed aqueous suspension of the prepared nanoparticles was applied and Zeta measurements was performed at pH value of 7.5. Each experiment was carried out in triplicate and data were presented as means  $\pm$  standard deviations. For fabricating an implant, the adequate mass of the synthesized CS-FA-MBZ nanoparticles (according

to the mouse body weight and its needed dosage of MBZ) were pressed in a steel die at 1500 psi to form cylindrical implants (usually 6 mm diameters and 3 mm height).

#### Cell viability assay

MTT assay was employed for the cell viability evaluation according to our previous studies [56, 65]. The 4T1

and L929 cells were separately seeded into 96-well culture plates at  $5 \times 10^3$  cells/well density. After 24 h incubation, different concentrations (0, 0.5, 1, and 1.5  $\mu\text{M}$ ) of MBZ, CS-FA, and CS-FA-MBZ were dissolved in culture medium and added to the wells. The cells were incubated for 48 h and then, the culture media was replaced with RPMI culture medium containing 0.005% MTT solution. After 4 h incubation in the standard cell culture incubator, the medium was discarded and the precipitated formazan crystals were dissolved in dimethyl sulfoxide (DMSO). At last, an absorbance Microplate Reader (BioTek-ELX800, USA) was used to measure the absorbance of the wells at 570 nm wavelength. Subsequently, the below-mentioned Eq. (3) was used to calculate the cell viability percentage of the treated wells in comparison with the control wells (0  $\mu\text{M}$ ). The experiment was repeated three times and at least six wells were used for each concentration.

$$\text{Cell viability}(\%) = \frac{(\text{OD Sample} - \text{OD Blank})}{(\text{OD Control} - \text{OD Blank})} \times 100. \quad (3)$$

#### Animal ethics, care, and handling

All animal experiments complied with the ARRIVE guidelines and were conducted according to the guidelines of the European Communities Council Directive (2010/63/UE) and the Isfahan University of Medical Sciences for the care and use of laboratory animals. Likewise, all the procedures, protocols, and steps were approved by the ethics committee of the Isfahan University of Medical Sciences (IR.MUI.RESEARCH.REC.1399.125). Female BALB/c mice (weight:  $25 \pm 2$  g) were purchased from the Pasteur Institute of Tehran, Iran. The mice were acclimatized to the laboratory environment ( $24 \pm 2$  °C temperature,  $50 \pm 10\%$  relative humidity, and 12 h light/12 h dark cycles) for 14 days before involving in the experiments. All mice were fed sterilized standard mouse chow and water ad libitum. Overdose of Ketamine-Xylazine (KX) solution through intraperitoneal injection was used for the mice sacrifice.

#### Tumor implantation

4T1 cancer cells (murine mammary carcinoma) were purchased from the Pasteur Institute of Tehran, Iran. The cells were cultured in RPMI 1640 medium containing 10% fetal bovine serum (FBS). The cells were incubated at 37 °C in a humidified incubator in 5%  $\text{CO}_2$  atmosphere. When the cells reached adequate numbers, they were harvested from culture flasks by trypsin and washed three times with PBS. The mice were injected with  $2 \times 10^6$  cells suspended in 50  $\mu\text{L}$  of FBS-free DMEM-F12,

subcutaneously (s.c.) into the left 4th abdominal mammary fat pad.

#### Tumor-bearing mice grouping and therapeutic approaches

For this experiment 32 tumor-bearing mice were used. When the tumors' volume reached 50–70  $\text{mm}^3$  (3rd day after the cancer cells injection), mice were divided into four groups ( $n=8$ ) including (1) Control, (2) MBZ (40 mg/kg, oral administration, twice a week for 2 weeks), (3) CS-FA implants, (4) CS-FA-MBZ implants. The tumor-bearing mice in the 2nd group were treated with oral administration p.o. (of MBZ (40 mg/kg, twice a week for 2 weeks according to previous studies [66]) from the 3rd day after the cancer cells injection. In the 3rd and 4th groups, the tumor-bearing mice were anesthetized with intraperitoneally injection of Ketamine-Xylazine (KX) solution (Ketamine: 100 mg/kg, Xylazine: 10 mg/kg). The left flank was shaved and scrubbed with betadine. The scrub solution was wiped away from the surgical site with alcohol 70% and covered with a sterile drape. Then, a small (~1 cm) incision was made and the implant was embedded under sterile conditions, and the skin was stitched with nylon (4–0). All the operations were done under complete anesthesia. To manage post-surgical pain, ketoprofen (5 mg/kg) was administered subcutaneously until the next 72 h. It should be mentioned that mice in the Control and MBZ group underwent the same surgery at the same day as two other groups and post-operative pain management protocol to prepare the same condition in all groups. The mice were monitored daily for prolonged signs of pain, weight loss, or surgical site infections. If any signs of pain, wounds infection, massive necrosis, and hemorrhage, diffuse metastasis were observed during any steps of the study, the mice were sacrificed by KX overdose. In the Control group, one incision was made at the left flank of the tumor-bearing mice and sutured without implantation of any implants. To determine tumors' growth progression, the greatest longitudinal diameter (length) and the greatest transverse diameter (width) of the tumors were measured every 3 days until the 18th after cancer cells injection. Then, the tumor's volume was calculated by the tumor volume Eq. (4). For survival analysis, the tumor-bearing mice were observed for 70 days after treatment administration. The animals' death was recorded every day. It should be mentioned that standardized humane endpoints based on the current guidelines for endpoints in animal tumor studies were used [67–69].

$$\text{Tumor volume} = \frac{(\text{Tumor length}) \times (\text{Tumor width})^2}{2} \quad (4)$$

#### 4T1 breast tumors' metastasis

For this experiment, 20 tumor-bearing mice were involved ( $n=5$ ) and the groups and therapeutic methods were completely the same as the previous section. The mice were sacrificed by overdose of ketamine/xylazine 30 days after cancer cell implantation and their livers were harvested and fixed in 10% neutral buffered formalin solution. An automatic tissue processor (Sakura, Japan) was employed to process the fixed samples. Then, a microtome (Leica Biosystems, Germany) was utilized to cut 4  $\mu\text{m}$  thickness serial sections from the paraffin-embedded blocks. The sections were stained with Hematoxylin & Eosin (H&E) staining protocol according to previous studies [57, 70]. A minimum of 10 random microscopic fields was observed under the  $10\times$  objective lens of a light microscope (Olympus, Japan) to report the mean number of metastatic colonies per microscopic field of the liver. Furthermore, the occupied area by metastatic colonies in each microscopic field of the liver (magnification  $\times 100$ ) was quantified by the Qupath software. The mean percentage of occupied space by liver metastatic colonies in each microscopic field was reported for each sample.

#### Histopathology and blood biochemical assays

For evaluating the safety of the subcutaneous CS-FA-MBZ implants, 20 healthy mice were involved and randomly divided into four groups ( $n=5$ ) including (1) Control, (2) MBZ, (3) CS-FA, and (4) CS-FA-MBZ implants according to the “Tumor-bearing mice grouping and therapeutic approaches” section. The mice were monitored for general appearance and behavioral parameters for 30 days. They were under close monitored for any signs of toxicity and behavioral changes including weakness, salivation, anorexia, diarrhea, aggressiveness, eyes and ears discharge, noisy breathing, activity, convulsion, cachexia, pain, or any signs of illness in each group for 30 days [71]. On the 30th day, the mice were sacrificed and blood urea nitrogen (BUN), creatinine (Cr), alanine aminotransferase (ALT), and aspartate aminotransferase (AST) levels were measured in the discarded serums [72]. In addition, lungs, kidneys, liver, and spleen were harvested and fixed, processed, and H&E stained. Histological photographs were obtained using a digital light microscope (Olympus, Japan).

#### Statistical analysis

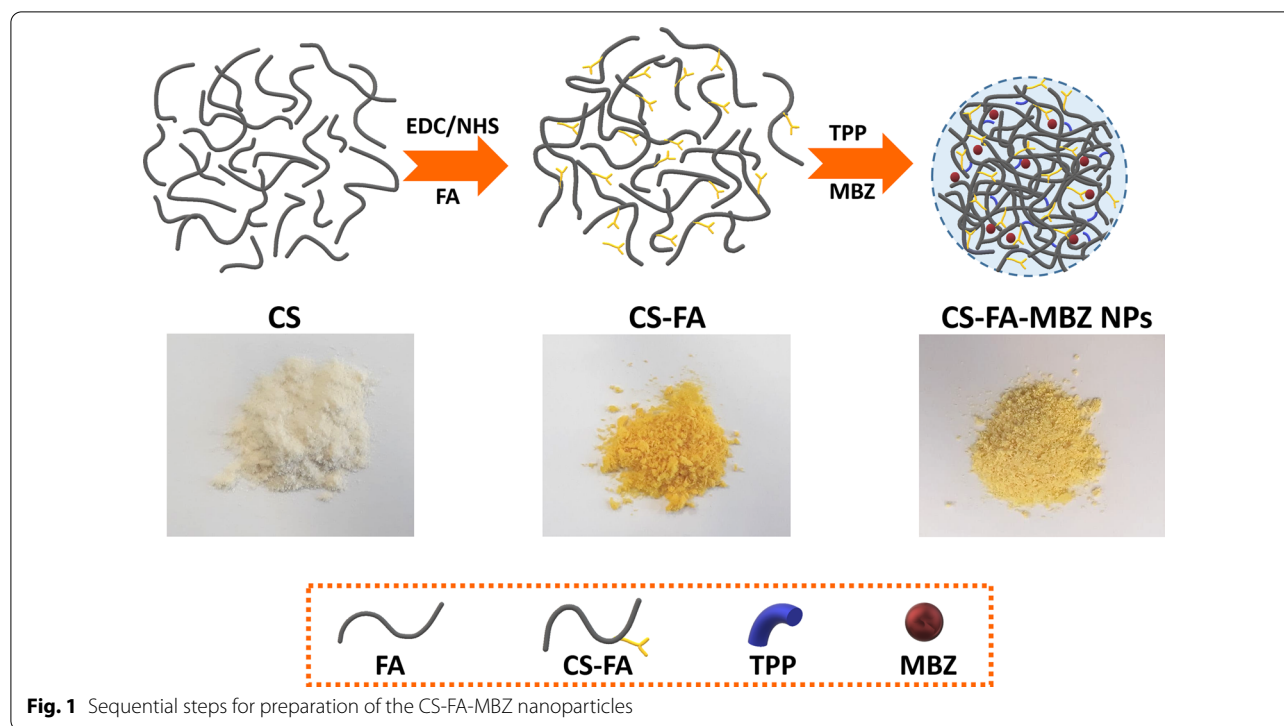
The statistical analyzes were performed using one-way analysis of variance (ANOVA) with Tukey's post-hoc test by JMP 14.0 software (SAS Institute, Japan). The results were statistically significant at  $P < 0.05$  (\*:  $P < 0.05$ , ns: not significant). All values were expressed as the mean  $\pm$  standard deviation.

## Results and discussion

### Fabrication and characterization of the CS-FA-MBZ nanoparticles

To fabricate CS-FA-MBZ nanoparticles, at first, folic acid was conjugated to chitosan in the presence of EDC as carboxyl activating agent to produce CS-FA (Additional file 1: Figure S1). The activated carboxyl moiety of FA was covalently linked to the amine groups of CS [73]. At the next step, the cross-linking reaction between CS-FA and TPP led to the formation of nanoparticles as the negatively charged TPP was electrostatically adsorbed to the positively charged free protonated amine groups of the CS-FA. Subsequently, MBZ was encapsulated during the synthesis process (Fig. 1).

The successful introduction of folate to CS chains was initially evaluated by FTIR (Fig. 2a). As shown in Fig. 2a, the characteristic bands of CS located at  $3422\text{ cm}^{-1}$  assigned to O–H stretching vibration overlapped with N–H stretching mode. The bands at  $2920$  and  $2880\text{ cm}^{-1}$  could be attributed to the C–H stretching vibrations of CS. Moreover, the peaks that appeared at  $1656$  and  $1605\text{ cm}^{-1}$  correspond to the C–O stretching vibration of amide I and N–H bending vibration of amide II, respectively [74]. FTIR spectrum of free FA showed characteristic bands located at  $1696$  and  $1640\text{ cm}^{-1}$  related to the C=O stretching vibration of the carboxyl group and N–H bending vibration of CONH, respectively [75]. In the CS-FA spectrum, the absorption peaks at  $1635$  and  $1031\text{ cm}^{-1}$  could be attributed to the vibration of C–N [74]. The amid band at  $1656\text{ cm}^{-1}$  of CS shifted to  $1635\text{ cm}^{-1}$  because of overlapping with the newly formed amide bond, and also a new N–H bending vibration located at  $1520\text{ cm}^{-1}$  confirmed the successful conjugation of FA to CS [76]. Moreover, UV–Vis spectra of CS, FA, and CS-FA are shown in Fig. 2b. CS had no absorption while the characteristic absorption bands of FA were appeared at  $280$  and  $350\text{ nm}$  which could be related to the typical  $\pi \rightarrow \pi^*$  transition of its pterin ring. CS-FA exhibited the FA absorption bands with a slight shift to longer wavelength ( $284$  and  $360\text{ nm}$ ) indicating the conjugation of CS to FA. Conjugation process was further demonstrated by  $^1\text{H-NMR}$  analysis (Fig. 2c). Signals appeared at  $\delta 1.85$ ,  $2.97$  and  $3.51\text{--}3.70\text{ ppm}$  which could be attributed to the resonance of the  $-\text{COCH}_3$ ,  $-\text{CH-NH-}$ , and  $-\text{CH}_2\text{-O-}$  groups in CS, respectively [77]. Presence of signals at  $\delta 2.54$  and  $2.65\text{ ppm}$  could be related to methylene groups of FA attached to the new amide bond [61, 76]. Moreover, the resonance of the folate aromatic protons observed at  $6.5\text{--}8.5\text{ ppm}$ , confirmed the successful conjugation of CS to FA. CS-FA was dissolved in deuterated acetic acid ( $\text{CD}_3\text{COOD}$ ) in  $\text{D}_2\text{O}$ . Therefore, the acetic peak was apparent at  $\delta 2.30\text{ ppm}$  [78]. Taken together, FTIR, UV–Vis, and  $^1\text{H-NMR}$  analyses verified



the successful conjugation process and their results were consistent with the previous studies [79].

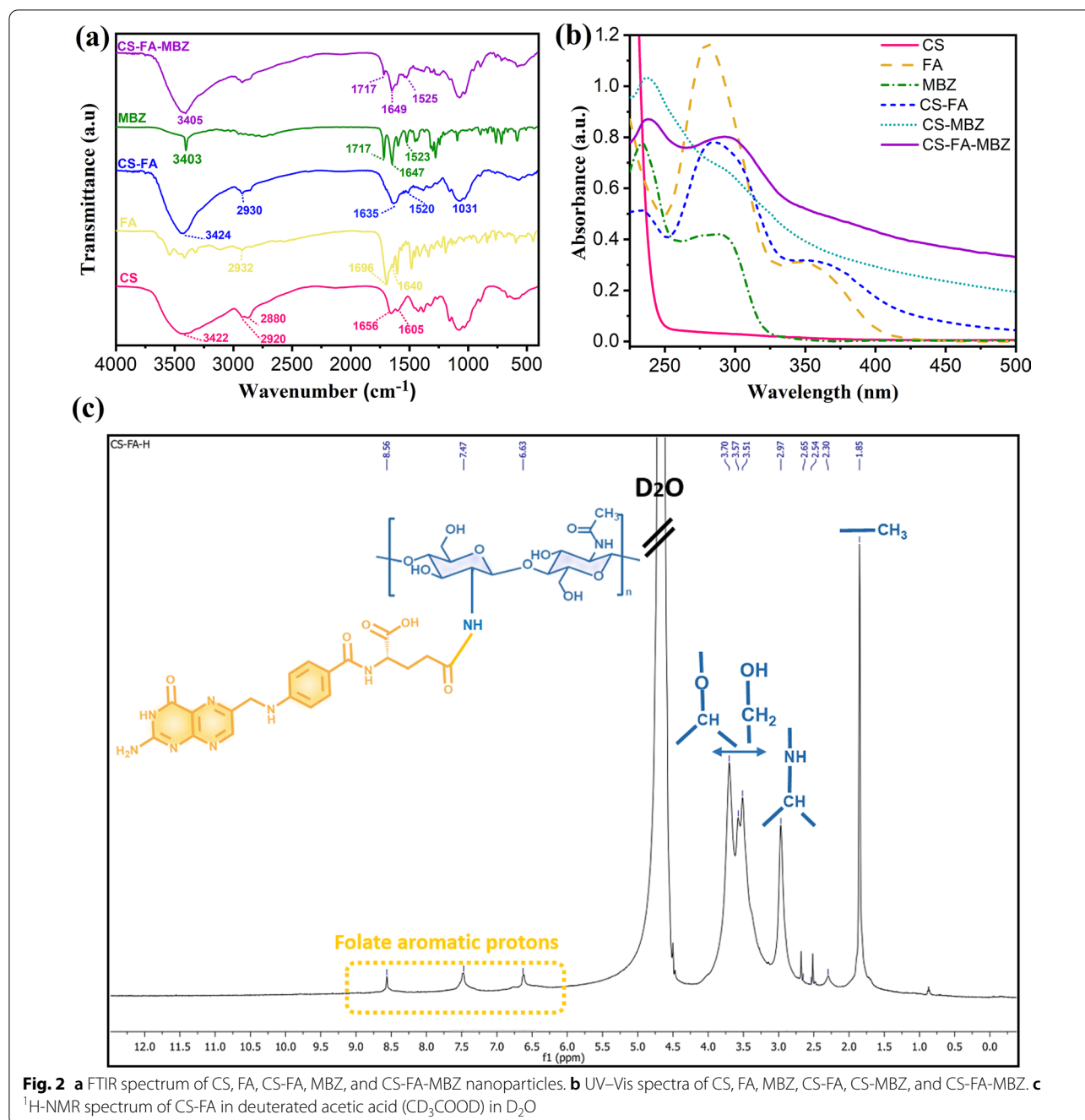
Thereafter, MBZ, as a hydrophobic drug, was loaded into the CS-FA nanoparticles (CS-FA-MBZ). FTIR and UV-Vis analyses were applied for verification of MBZ loading as well. FTIR results (Fig. 2a) showed the N-H stretching and bending vibrations of MBZ at 3403 and 1523  $\text{cm}^{-1}$  which were observed for CS-FA-MBZ at 3405 and 1525  $\text{cm}^{-1}$ , respectively. Furthermore, the stretching vibration of amide I of the carbamate group of MBZ (1717  $\text{cm}^{-1}$ ) appeared at the CS-FA-MBZ nanoparticles spectrum in the same location, indicating successful MBZ loading [80]. The UV-Vis spectrum of MBZ (Fig. 2b) showed the characteristic absorption band at 234 nm which was observed for CS-MBZ as well. This band along with the absorption band of FA at  $\sim 280$  nm with a slight shift to longer wavelengths was detected in the spectrum of CS-FA-MBZ, indicating the appropriate MBZ loading into the CS-FA nanoparticles.

Figure 3a and b show SEM images of the CS-FA-MBZ at different magnifications, in which the nanoparticles were uniform, with mainly spherical morphology. Figure 3c shows the corresponding particle size distribution histograms (dry state) obtained by measuring the size of 100 nanoparticles in the SEM images by the “Image J” software. A narrow size distribution with a mean size of  $153.3 \pm 18.4$  nm was measured. Moreover, the particle size distribution of the CS-FA-MBZ was determined by

DLS measurement (wet state). The hydrodynamic diameter of the nanoparticles was measured  $182 \pm 12.1$  nm (Additional file 1: Figure S2) with a low polydispersity index ( $\text{PDI} < 0.2$ ) illustrating a narrow size distribution which was consistent with the results obtained from the SEM. In addition, TEM images of CS-FA-MBZ nanoparticles are shown in Fig. 3d. The zeta potential distribution histograms of CS, CS-FA and CS-FA-MBZ at pH value of 7.5, exhibit that the positive charge of chitosan due to the presence of the amine groups decreases with the conjugation of FA (Fig. 3e). It can be attributed to the interaction of FA molecules with these amine groups of CS leading to the neutralization of the potential value [81]. Additionally, the results depict that the encapsulation of MBZ into the CS-FA nanoparticles induces a noticeable change of zeta value of the final nanoparticles with the preserved positive value of +27 mV.

#### MBZ loading

After successful loading of MBZ into CS-FA nanoparticles (Fig. 2a, b), the encapsulation efficacy (EE) and loading capacity (LC) of MBZ were calculated by plotting the standard calibration curve with a linear curve fit equation (Additional file 1: Figure S3). The value of EE and LC were 57.7% and 10.5%, respectively. This fact demonstrates the valuable capability of the target system for MBZ loading.



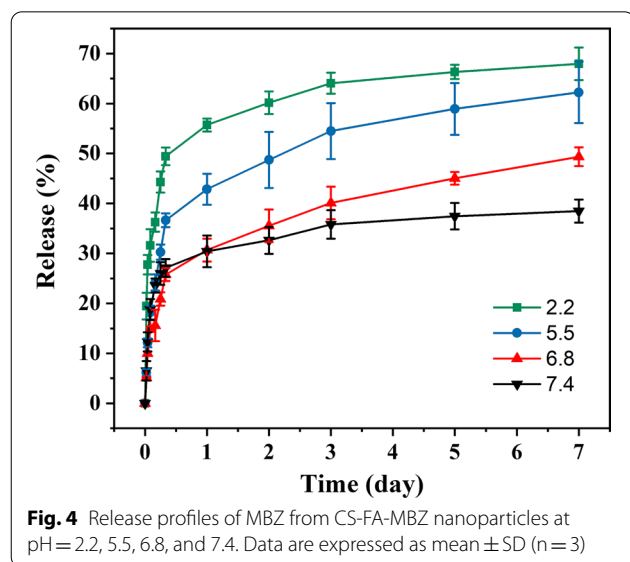
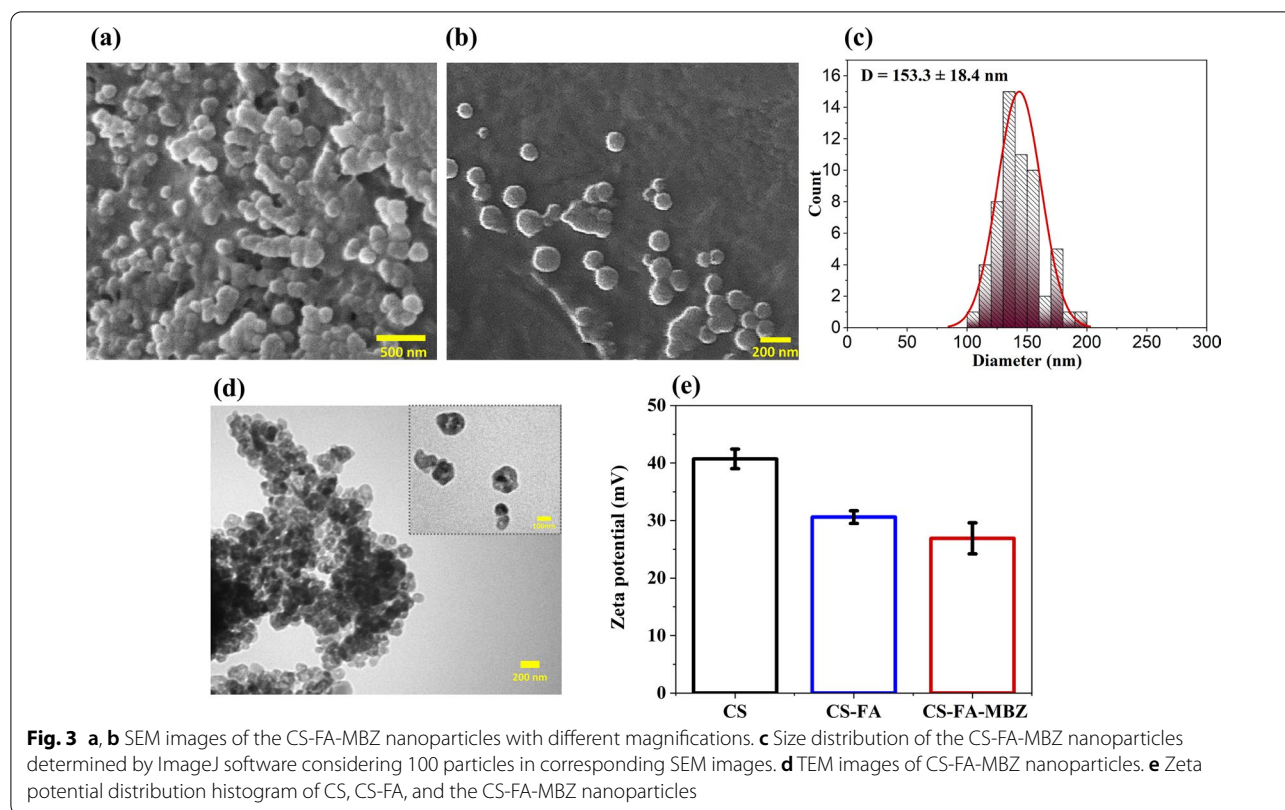
**Fig. 2** **a** FTIR spectrum of CS, FA, CS-FA, MBZ, and CS-FA-MBZ nanoparticles. **b** UV-Vis spectra of CS, FA, MBZ, CS-FA, CS-MBZ, and CS-FA-MBZ. **c** <sup>1</sup>H-NMR spectrum of CS-FA in deuterated acetic acid (CD<sub>3</sub>COOD) in D<sub>2</sub>O

### In vitro MBZ release pattern

The release pattern of MBZ from CS-FA-MBZ was evaluated at different pH values including, 2.2, 5.5, 6.8, and 7.4 to mimic various microenvironments. The MBZ release pattern was monitored at different time points including, 0.5 h, 1 h, 2 h, 4 h, 6 h, 8 h, 1 day, 2 days, 3 days, 5 days, and 7 days after immersing the CS-FA-MBZ nanoparticles in PBS according to previous

studies [64]. As Fig. 4 illustrates, the CS-FA-MBZ nanoparticles exhibited a continuous and sustained MBZ release profile at different pH values started with a burst release within 6 h followed by a gradual release within the next 7 days. The initial fast release could be related to the MBZ loaded near the surface of nanoparticles [75]. Besides, the CS-FA-MBZ nanoparticles revealed a pH-responsive behavior for MBZ release. At the 7th day, the release of MBZ was ~68%, 62%, 49%, and 38%





at pH values of 2.2, 5.5, 6.8, and 7.4, respectively. This behavior could be assigned to the high swelling ability of CS which was induced by protonation of the amine groups of the polymer in the acidic environment [75]. Considering the acidic microenvironment of cancerous tissues, the pH-sensitive behavior of the CS-FA-MBZ

nanoparticles can improve their capability for tumor-specific drug release. The pH-sensitive property of the CS-FA-MBZ nanoparticles can accelerate MBZ release in the acidic microenvironment of tumor while avoids its premature release in the normal tissues' microenvironment which can reduce the probable adverse effects to the normal tissues[82].

#### Cytotoxic effect of CS-FA-MBZ nanoparticles on the breast cancer and normal cells

The 4T1 murine triple-negative mammary cancer and L929 normal murine fibroblast cell lines were treated with different concentrations (0, 0.5, 1, and 1.5  $\mu$ M) of MBZ, CS-FA, CS-FA-MBZ nanoparticles. As Fig. 5 illustrates, MBZ and CS-FA nanoparticles exhibit anti-cancer properties which is dose dependent. On the other hand, the most significant decrease in the 4T1 cancer cells viability percentage was observed in the highest dose of the CS-FA-MBZ nanoparticles-treated wells which demonstrates the increased anti-cancer effectiveness of MBZ after loading in the CS-FA platform. This can be attributed to the folic acid targeting of the nanoparticles which increases the internalization of loaded MBZ into the cancer cells and also, the anti-cancer effect of CS nanoparticles per se which is consistent with the previous

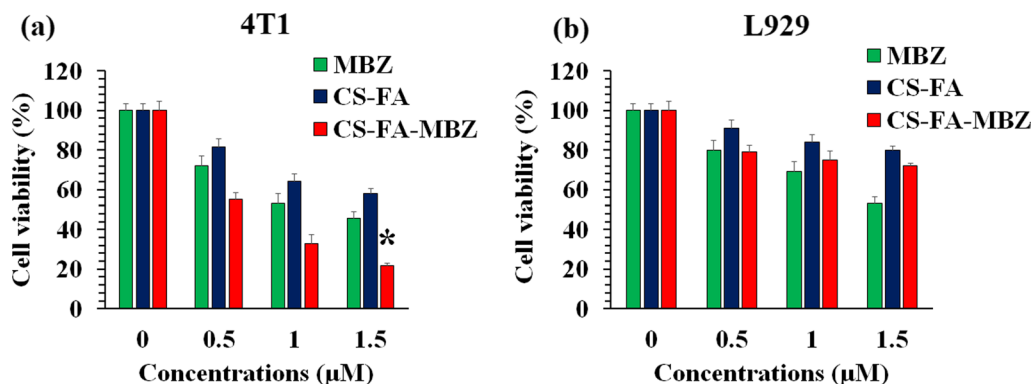


**Fig. 5** Cytotoxic effect of different concentrations (0, 0.5, 1, and 1.5 μM) of MBZ, CS-FA, and CS-FA-MBZ nanoparticles on **a** 4T1 breast cancer and **b** L929 normal cells viability after 48 h incubation according to MTT assay

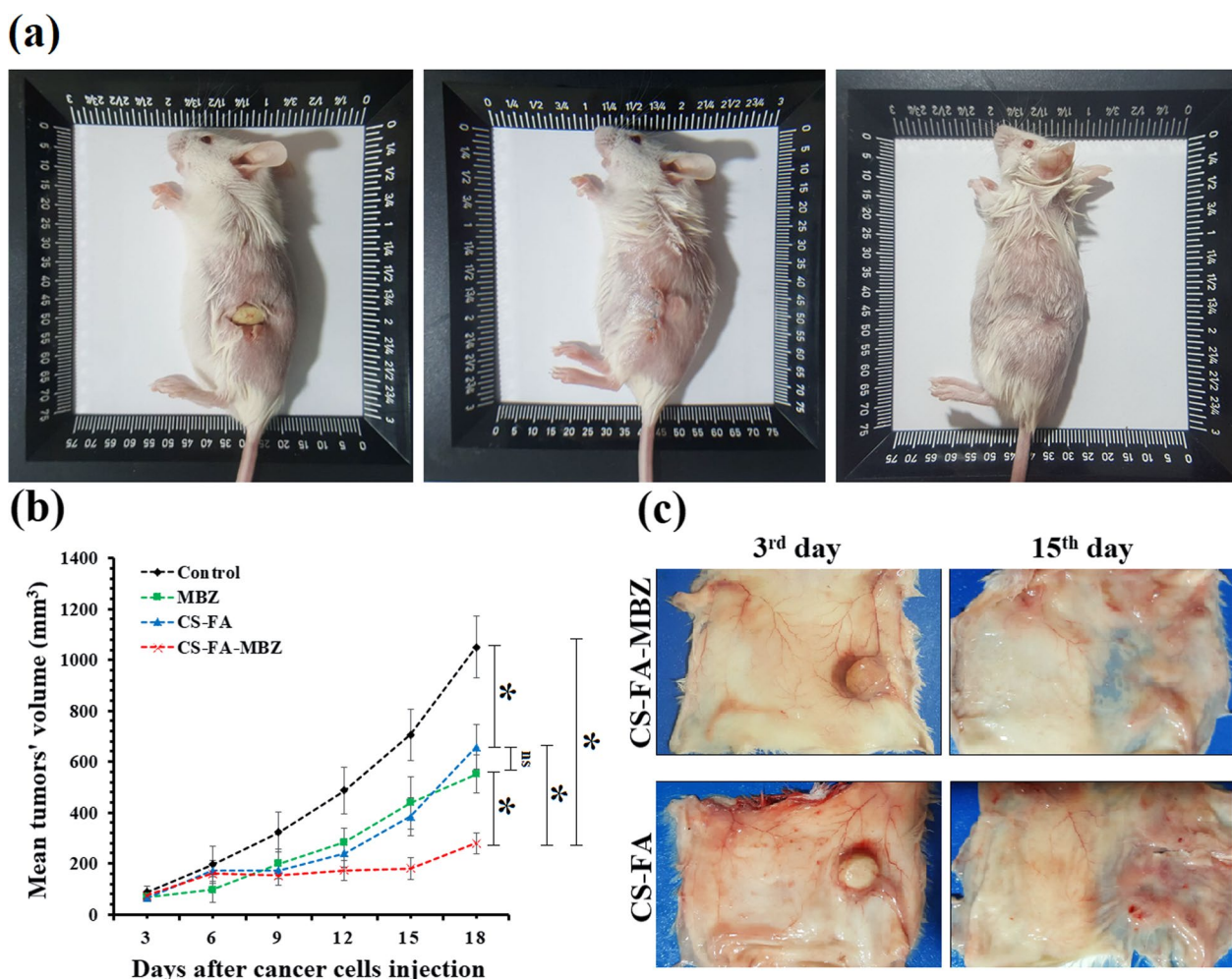


**Fig. 6** **a** Subcutaneous implantation of the CS-FA-MBZ implants. A small incision was made at the left flank of mice and the implant was placed inside it. The incision was sutured. The implantation site on the 18th day after cancer cells injection (15th day after surgery). **b** Tumors' growth progression in different groups including Control, MBZ, CS-FA, and CS-FA-MBZ from the 3rd to 18th day after cancer cells injection (not significant: ns, \*:  $P < 0.05$ ). **c** Harvested skin of the implants-bearing mice at the 3rd and 15th days after implantation which equates the 6th and 18th days after cancer cells injection, respectively

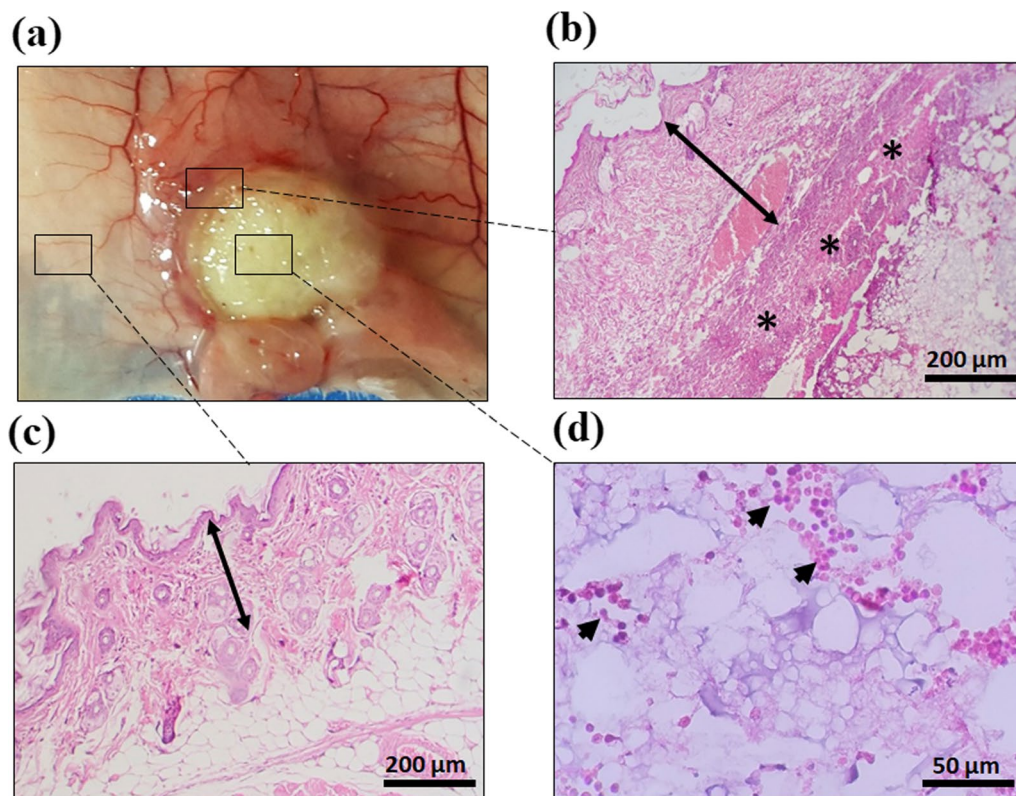


**Fig. 7** Mouse body response to the subcutaneously implanted CS-FA-MBZ at 3rd day after implantation according to histopathology analysis. **a** A close-up view of a CS-FA-MBZ implant 3rd day after implantation and histopathological evaluation of **b** the implant-surrounding membrane, **c** tissues far away from the implantation site, and **d** tissues at the bed of the implantation site. The two head arrows, asterisk, and one-head arrows indicate derma, the implant's surrounding membrane, and infiltrating immune cells, respectively

publications [83]. Taking together, CS-FA-MBZ exhibits not only significantly more cytotoxic effects on the 4T1 cancer cells in comparison with the CS-FA nanoparticles or pure MBZ but also, lower toxicity on the L929 normal cells rather than MBZ.

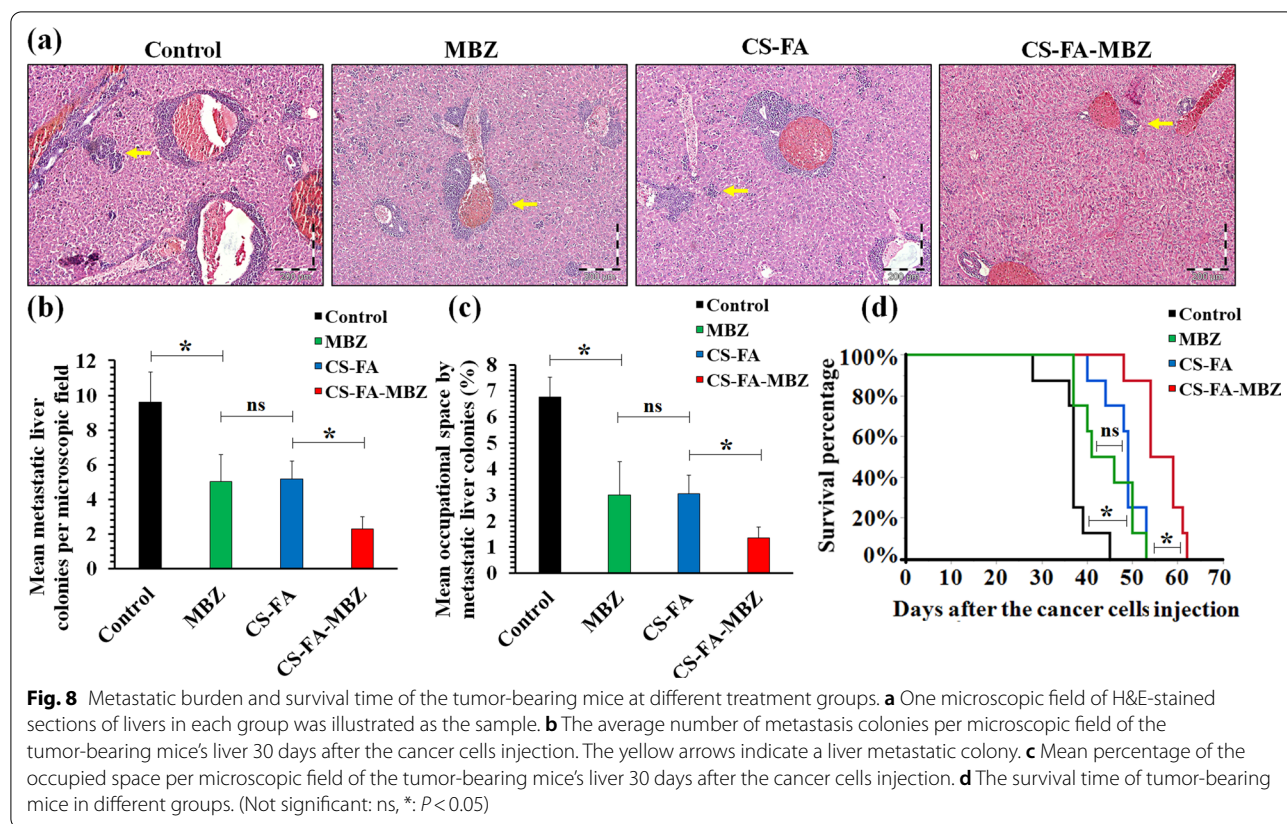
#### The CS-FA-MBZ implants effect on the 4T1 breast tumors' growth progression

As Fig. 6a illustrates, the CS-FA and CS-FA-MBZ implants were s.c. implanted in the left flank of the tumor-bearing mice inside a small incision on the 3<sup>rd</sup> day after the cancer cell injection. The implants were completely palpable even after suturing the incision. The implants completely degraded until the 18th day in both CS-FA and CS-FA-MBZ groups and nothing was palpable at the implantation site. This means that the implants were dissociated and release their composing agents means CS-FA-MBZ nanoparticle.

The therapeutic effect of the CS-FA-MBZ implants on inhibition of 4T1 tumors' growth progression was evaluated by serial measurement of tumor's diameters and compared with the Control, MBZ (40 mg/kg, oral

administration, twice a week for 2 weeks), and CS-FA groups (Fig. 6b). All treatments were initiated from the 3rd day after cancer cells injection. As Fig. 6b illustrates, the CS-FA-MBZ implants could significantly inhibit the breast tumors growth progression in comparison with all other groups. On the last day of tumors' volume monitoring (18th day after cancer cells injection), the mean tumors' volume at the CS-FA-MBZ group ( $280.6 \pm 42.2 \text{ mm}^3$ ) was significantly ( $P < 0.05$ ) lower than the Control ( $1050.5 \pm 120.7 \text{ mm}^3$ ), MBZ ( $552.4 \pm 76.1 \text{ mm}^3$ ), and CS-FA ( $658.3 \pm 88.1 \text{ mm}^3$ ) groups. The CS-FA-MBZ implants caused about 73.3%, 49.2%, 57.4% decrease in the mean tumors' volume in comparison with the Control, MBZ, and CS-FA groups, respectively. Therefore, CS-FA-MBZ implants exhibit high efficacy in inhibiting breast tumors growth.

On the 6th and 18th days (3rd and 15th days after surgery, respectively), some implants-bearing mice were sacrificed to observe what is happening on the CS-FA and CS-FA-MBZ implants' site (Fig. 6c). As illustrated in Fig. 6c, the implants were surrounded by



a thin transparent membrane on the 6th day. On the 18th day, the implants were completely degraded and disappeared. As Fig. 7 illustrates, histopathological evaluations of the implantation site on the 6th day demonstrated that the surrounding membrane consisted of connective tissue. Also, limited mononuclear cells infiltration was observed at the implants' bed (Fig. 7).

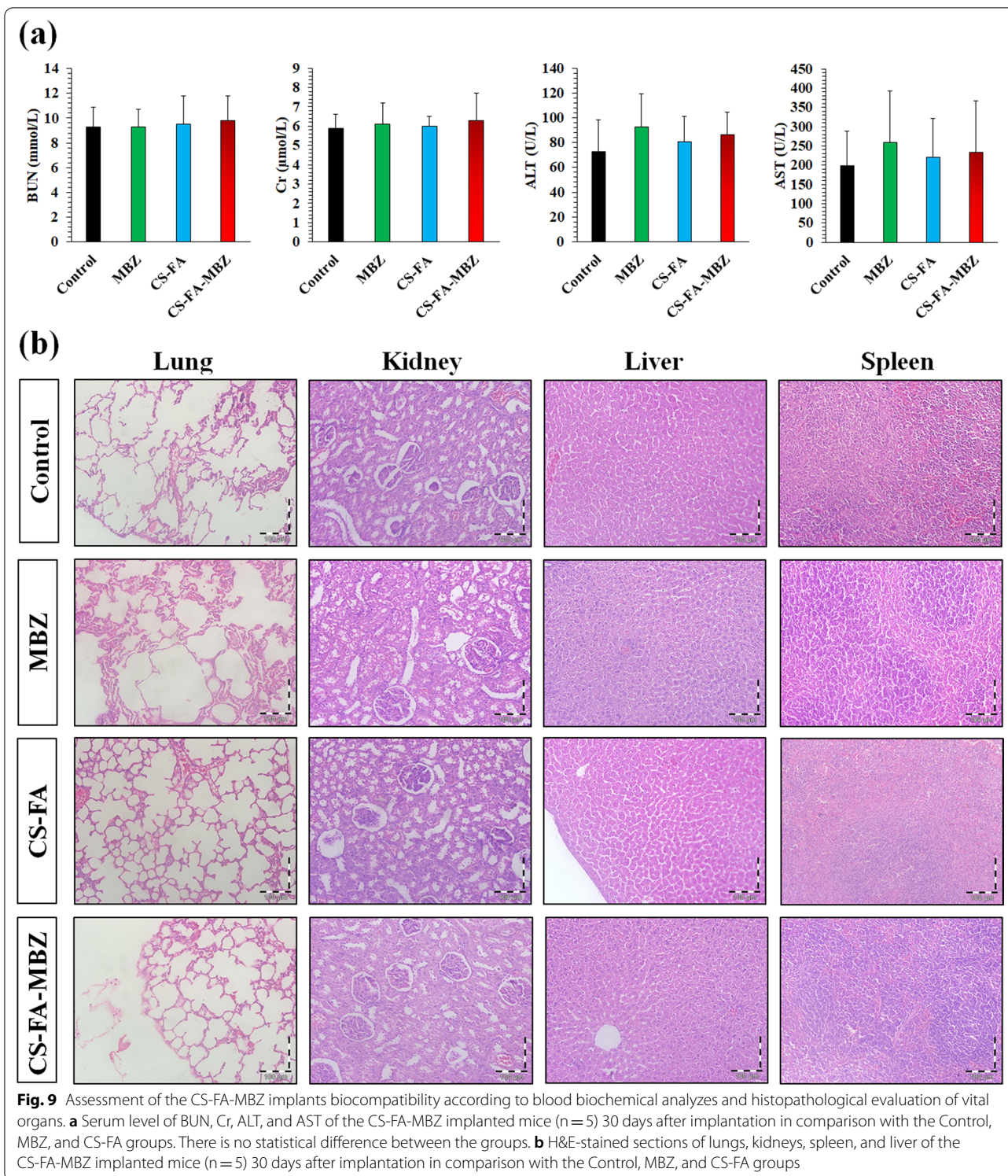
#### The CS-FA-MBZ implants effect on metastasis and tumor-bearing mice survival time

Metastasis is the main cause of cancer-related deaths. The formation of metastatic colonies at vital organs like the liver disrupts their function and causes organ failure [84]. Therefore, to evaluate the effect of the CS-FA-MBZ implants on metastasis formation, H&E sections were used to count the metastatic colonies at tumor-bearing mice liver after 35 days from cancer cells injection (Fig. 8). Histopathological evaluations demonstrated significant inhibition of the liver metastatic colonies formation at the CS-FA-MBZ ( $2.3 \pm 0.7$ ) treated mice in comparison with the Control ( $9.6 \pm 1.7$ ), MBZ ( $5.0 \pm 1.5$ ), and CS-FA ( $5.2 \pm 1$ ) groups (Fig. 8a and b). Besides, the metastatic colonies occupied significantly ( $P < 0.05$ ) lower space in the liver sections (per

microscopic field) of the CS-FA-MBZ treated group in comparison with the other groups (Fig. 8c). In addition, the CS-FA-MBZ group exhibited about 52.1%, 27.3%, and 17% more survival time (days) in comparison with the Control, MBZ, and CS-FA groups, respectively (Fig. 8d). This increase in the tumor-bearing mice survival time can be attributed to significant inhibition of 4T1 tumors' growth and metastasis.

#### Biocompatibility of the subcutaneous CS-FA-MBZ implants

The safety and biocompatibility of implants are very important for clinical application. Therefore, the CS-FA-MBZ implants' safety and biocompatibility were evaluated in comparison with the Control, MBZ, CS-FA group in non-tumor-bearing mice. The treatment protocol was the same as "Tumor-bearing mice grouping and therapeutic approaches" section for each group. The mice were exactly monitored according to general appearance and behavioral parameters, blood biochemical analyzes, and histopathological evaluation of vital organs. No sign of change in the mice's appearance, behavioral pattern, and food intake were observed during the 30 days (Additional file 1: Tables S1) in none of the groups. On the 30th day, the animals were sacrificed and their plasma was collected for biochemical (Fig. 9a)



analyses and the vital organs were harvested for histopathological exams (Fig. 9b). No significant sign of organ damage was observed in either H&E sections and blood biochemical analyzes. Chitosan nanoparticles

are the main component of CS-FA-MBZ implants. Chitosan is a natural biodegradable biopolymer. The enzymatic degradation of chitosan causes its transformation to some components which are completely safe. Many

enzymes have the ability to degrade chitosan and the most well-known one is lysozyme as a non-specific protease. This enzyme which presents in all mammalian tissues and fluids, plays a key role in degradation of chitosan-based implants *in vivo*. It targets the acetylated residues of chitosan polymer and degrades chitosan to non-toxic oligosaccharides which can be excreted or incorporated to glycosaminoglycans and glycoproteins [30, 85–87]. Also, eight human chitinases (in the glycoside hydrolase 18 family) have been identified, three of which have shown enzymatic activity [88]. On the other hand, in the MBZ group which were under treatment with oral administration of MBZ a mild increase in the liver enzymes was observed which is a routine side effect of MBZ [89]. This can be related to the hepatotoxic effect of MBZ which was not detected at the CS-FA-MBZ implants groups. Taking together, CS-FA-MBZ implants system can decrease the side effects of MBZ and cause significant therapeutic efficacy in the TNBC tumor-bearing mice.

## Conclusions

Chemotherapy drugs loaded implants have exhibited higher efficacy in comparison with common routes of drug administration. In the present study, folic acid-targeted chitosan nanoparticles were used as a carrier to increase MBZ therapeutic efficacy in the triple-negative breast cancer-bearing BALB/c model. A definite amount of MBZ-loaded CS-FA nanoparticles were compressed to form cylindrical CS-FA-MBZ implants which were subcutaneously implanted at mice's flank. The CS-FA-MBZ implants could significantly inhibit 4T1 breast tumor growth and metastasis. Therefore, these biodegradable and biocompatible implants can be an appropriate choice for further experiments in breast cancer and other cancers treatment.

## Abbreviations

TNBC: Triple-negative breast cancer; MBZ: Mebendazole; FA: Folic acid; CS: Chitosan; KX: Ketamine-xylazine.

## Supplementary Information

The online version contains supplementary material available at <https://doi.org/10.1186/s12951-022-01380-2>.

**Additional file 1: Figure S1.** Schematic illustration of folic acid conjugation to chitosan in presence of EDC as carboxyl activating agent to produce CS-FA. **Figure S2.** The CS-FA-MBZ nanoparticles hydrodynamic size distribution according to DLS measurements. **Figure S3.** Standard calibration curve of MBZ. **Table S1.** General appearance and behavioral observations for Control and CS-Fa-MBZ groups (n = 5).

## Authors' contributions

The study was designed by AK. *In vivo* assessments were carried out by AK and FG. The nanoparticles synthesis and characterization were done by

MH. The manuscript writing and revisions were done by AK, MH, FG, NAJ and MR. All the authors read and approved the final manuscript.

## Funding

This research was supported by Isfahan University of Medical Sciences.

## Availability of data and materials

All datasets are available upon reasonable request.

## Declarations

### Ethics approval and consent to participate

All animal experiments complied with the ARRIVE guidelines and were conducted according to the guidelines of the European Communities Council Directive (2010/63/UE) and the Isfahan University of Medical Sciences for the care and use of laboratory animals. Likewise, all the procedures, protocols, and steps were approved by the ethics committee of the Isfahan University of Medical Sciences (IR.MUI.RESEARCH.REC.1399.125).

### Consent for publication

All authors have read and agreed to publish this manuscript.

### Competing interests

The authors declared no potential competing interests with respect to the research, authorship, and/or publication of this article.

### Author details

<sup>1</sup>Cancer Prevention Research Center, Department of Oncology, Isfahan University of Medical Sciences, 81746-73461 Isfahan, Iran. <sup>2</sup>Department of Chemistry, Amirkabir University of Technology (Tehran Polytechnic), 1591634311 Tehran, Iran. <sup>3</sup>Department of Medical Physics and Radiotherapy, School of Paramedicine, Arak University of Medical Sciences, Arak, Iran. <sup>4</sup>Biosensor Research Center, Isfahan University of Medical Sciences, Isfahan, Iran.

Received: 7 January 2022 Accepted: 17 March 2022

Published online: 31 March 2022

## References

- DeSantis CE, et al. Breast cancer statistics, 2017, racial disparity in mortality by state. *CA Cancer J Clin.* 2017;67(6):439–48.
- Perou CM, et al. Molecular portraits of human breast tumours. *Nature.* 2000;406(6797):747–52.
- Kumar P, Aggarwal R. An overview of triple-negative breast cancer. *Arch Gynecol Obstet.* 2016;293(2):247–69.
- Wang J, et al. Adjuvant chemotherapy and radiotherapy in triple-negative breast carcinoma: a prospective randomized controlled multi-center trial. *Radiother Oncol.* 2011;100(2):200–4.
- Sorolla A, et al. Triple-hit therapeutic approach for triple negative breast cancers using docetaxel nanoparticles, EN1-iPeps and RGD peptides. *Nanomed Nanotechnol Biol Med.* 2019;20:102003.
- Al-Mahmood S, et al. Metastatic and triple-negative breast cancer: challenges and treatment options. *Drug Deliv Transl Res.* 2018;8(5):1483–507.
- Nedeljković M, Damjanović A. Mechanisms of chemotherapy resistance in triple-negative breast cancer—how we can rise to the challenge. *J Cells.* 2019;8(9):957.
- Guerini AE, et al. Mebendazole as a candidate for drug repurposing in oncology: an extensive review of current literature. *Cancers.* 2019;11(9):1284.
- Coyne CP, Jones T, Bear R. Gemcitabine-(C4-amide)-[anti-HER2/neu] anti-neoplastic cytotoxicity in dual combination with mebendazole against chemotherapeutic-resistant mammary adenocarcinoma. *J Clin Exp Oncol.* 2013;2(2):1000109.
- Doudican N, et al. Mebendazole induces apoptosis via Bcl-2 inactivation in chemoresistant melanoma cells. *Mol Cancer Res.* 2008;6(8):1308–15.
- Larsen AR, et al. Repurposing the antihelminthic mebendazole as a hedgehog inhibitor. *Mol Cancer Ther.* 2015;14(1):3–13.

12. Bai RY, et al. Brain penetration and efficacy of different mebendazole polymorphs in a mouse brain tumor model. *Clin Cancer Res.* 2015;21(15):3462–70.
13. He L, et al. Mebendazole exhibits potent anti-leukemia activity on acute myeloid leukemia. *Exp Cell Res.* 2018;369(1):61–8.
14. Mukhopadhyay T, et al. Mebendazole elicits a potent antitumor effect on human cancer cell lines both in vitro and in vivo. *Clin Cancer Res.* 2002;8(9):2963–9.
15. Pantziarka P, et al. Repurposing Drugs in Oncology (ReDO)—mebendazole as an anti-cancer agent. *ecancer.* 2014. <https://doi.org/10.3332/ecancer.2014.485>.
16. Martarelli D, et al. Mebendazole inhibits growth of human adrenocortical carcinoma cell lines implanted in nude mice. *Cancer Chemother Pharmacol.* 2008;61(5):809–17.
17. Pinto LC, et al. Mebendazole, an antiparasitic drug, inhibits drug transporters expression in preclinical model of gastric peritoneal carcinomatosis. *Toxicol In Vitro.* 2017;43:87–91.
18. Sung SJ, et al. Autophagy is a potential target for enhancing the anti-angiogenic effect of mebendazole in endothelial cells. *Biomol Ther.* 2019;27(1):117.
19. Bai RY, et al. Effective treatment of diverse medulloblastoma models with mebendazole and its impact on tumor angiogenesis. *Neuro Oncol.* 2015;17(4):545–54.
20. Dawson M, Allan R, Watson T. The pharmacokinetics and bioavailability of mebendazole in man: a pilot study using [3H]-mebendazole. *Br J Clin Pharmacol.* 1982;14(3):453–5.
21. Dawson M, et al. The pharmacokinetics and bioavailability of a tracer dose of [3H]-mebendazole in man. *Br J Clin Pharmacol.* 1985;19(1):79–86.
22. de la Torre-Iglesias PM, et al. Enhanced bioavailability and anthelmintic efficacy of mebendazole in redispersible microparticles with low-substituted hydroxypropylcellulose. *Drug Des Devel Ther.* 2014;8:1467–79.
23. Belz JE, et al. Sustained release talazoparib implants for localized treatment of BRCA1-deficient breast cancer. *Theranostics.* 2017;7(17):4340.
24. Park C-W, et al. In vitro/in vivo evaluation of NCDS-micro-fabricated biodegradable implant. *Arch Pharmacol Res.* 2010;33(3):427–32.
25. Arias JL. Novel strategies to improve the anticancer action of 5-fluorouracil by using drug delivery systems. *Molecules.* 2008;13(10):2340–69.
26. Weinberg BD, Blanco E, Gao J. Polymer implants for intratumoral drug delivery and cancer therapy. *J Pharm Sci.* 2008;97(5):1681–702.
27. Talebian S, et al. Biopolymers for antitumor implantable drug delivery systems: recent advances and future outlook. *Adv Mater.* 2018;30(31):e1706665.
28. Zhang Z, et al. Sandwich-like fibers/sponge composite combining chemotherapy and hemostasis for efficient postoperative prevention of tumor recurrence and metastasis. *Adv Mater.* 2018;30(49):e1803217.
29. Kuang G, et al. Biphasic drug release from electrospun polyblend nanofibers for optimized local cancer treatment. *Biomater Sci.* 2018;6(2):324–31.
30. Kefayat A, Vaezifar S. Biodegradable PLGA implants containing doxorubicin-loaded chitosan nanoparticles for treatment of breast tumor-bearing mice. *Int J Biol Macromol.* 2019;136:48–56.
31. Nam KS, Shon YH. Suppression of metastasis of human breast cancer cells by chitosan oligosaccharides. *J Microbiol Biotechnol.* 2009;19(6):629–33.
32. Li Y, et al. Chitosan sulfate inhibits angiogenesis via blocking the VEGF/VEGFR2 pathway and suppresses tumor growth in vivo. *Biomater Sci.* 2019;7(4):1584–97.
33. Adhikari HS, Yadav PN. Anticancer activity of chitosan, chitosan derivatives, and their mechanism of action. *Int J Biomater.* 2018. <https://doi.org/10.1155/2018/2952085>.
34. Unsoy G, et al. Synthesis of Doxorubicin loaded magnetic chitosan nanoparticles for pH responsive targeted drug delivery. *Eur J Pharm Sci.* 2014;62:243–50.
35. Tiyaboonchai W. Chitosan nanoparticles: a promising system for drug delivery. *Naresuan Univ J.* 2013;11(3):51–66.
36. Wang JJ, et al. Recent advances of chitosan nanoparticles as drug carriers. *J Int J Nanomed.* 2011;6:765.
37. Min KH, et al. Hydrophobically modified glycol chitosan nanoparticles-encapsulated camptothecin enhance the drug stability and tumor targeting in cancer therapy. *J Control Release.* 2008;127(3):208–18.
38. Nagpal K, Singh SK, Mishra DN. Chitosan nanoparticles: a promising system in novel drug delivery. *Chem Pharm Bull.* 2010;58(11):1423–30.
39. Sinha V, et al. Chitosan microspheres as a potential carrier for drugs. *Int J Pharm.* 2004;274(1–2):1–33.
40. Pan Y, et al. Bioadhesive polysaccharide in protein delivery system: chitosan nanoparticles improve the intestinal absorption of insulin in vivo. *Int J Pharm.* 2002;249(1–2):139–47.
41. Mitra S, et al. Tumour targeted delivery of encapsulated dextran–doxorubicin conjugate using chitosan nanoparticles as carrier. *J Control Release.* 2001;74(1–3):317–23.
42. Sahu SK, et al. In vitro evaluation of folic acid modified carboxymethyl chitosan nanoparticles loaded with doxorubicin for targeted delivery. *J Mater Sci Mater Med.* 2010;21(5):1587–97.
43. Yang SJ, et al. Folic acid-conjugated chitosan nanoparticles enhanced protoporphyrin IX accumulation in colorectal cancer cells. *Bioconjug Chem.* 2010;21(4):679–89.
44. Zhang S, et al. Synthesis and evaluation of clickable block copolymers for targeted nanoparticle drug delivery. *Mol Pharm.* 2012;9(8):2228–36.
45. Kularatne SA, Low PS. Targeting of nanoparticles: folate receptor. In: *Cancer Nanotechnology.* Berlin: Springer; 2010. p. 249–65.
46. Xu L, et al. Folate-mediated chemotherapy and diagnostics: an updated review and outlook. *J Control Release.* 2017;252:73–82.
47. Kefayat A, et al. Ultra-small but ultra-effective: folic acid-targeted gold nanoclusters for enhancement of intracranial glioma tumors' radiation therapy efficacy. *Nanomedicine.* 2019;16:173–84.
48. Kefayat A, et al. Investigation of different targeting decorations effect on the radiosensitizing efficacy of albumin-stabilized gold nanoparticles for breast cancer radiation therapy. *Eur J Pharm Sci.* 2019;130:225–33.
49. Foroushani MS, et al. Folate-graphene chelate manganese nanoparticles as a theranostic system for colon cancer MR imaging and drug delivery: in-vivo examinations. *J Drug Deliv Sci Technol.* 2019;54:101223.
50. O'Shannessy DJ, et al. Folate receptor alpha (FRA) expression in breast cancer: identification of a new molecular subtype and association with triple negative disease. *Springerplus.* 2012;1(1):22.
51. Zhang Z, et al. Folate receptor alpha associated with triple-negative breast cancer and poor prognosis. *Arch Pathol Lab Med.* 2014;138(7):890–5.
52. Necela BM, et al. Folate receptor- $\alpha$  (FOLR1) expression and function in triple negative tumors. *PLoS ONE.* 2015. <https://doi.org/10.1371/journal.pone.0122209>.
53. Paulmurugan R, et al. Folate receptor-targeted polymeric micellar nanocarriers for delivery of orlistat as a repurposed drug against triple-negative breast cancer. *Mol Cancer Ther.* 2016;15(2):221–31.
54. Kaur P, et al. A mouse model for triple-negative breast cancer tumor-initiating cells (TNBC-TICs) exhibits similar aggressive phenotype to the human disease. *BMC Cancer.* 2012;12(1):120.
55. Pulaski BA, Ostrand-Rosenberg S. Mouse 4T1 breast tumor model. *Curr Protoc Immunol.* 2000;39(1):20.2.1–20.2.16.
56. Ghahremani F, et al. AS1411 aptamer conjugated gold nanoclusters as a targeted radiosensitizer for megavoltage radiation therapy of 4T1 breast cancer cells. *RSC Adv.* 2018;8(8):4249–58.
57. Ghahremani F, et al. AS1411 aptamer-targeted gold nanoclusters effect on the enhancement of radiation therapy efficacy in breast tumor-bearing mice. *Nanomedicine.* 2018;13(20):2563–78.
58. Wei X, et al. 3D printed core-shell hydrogel fiber scaffolds with NIR-triggered drug release for localized therapy of breast cancer. *Int J Pharm.* 2020;580:119219.
59. Obayemi JD, et al. Degradable porous drug-loaded polymer scaffolds for localized cancer drug delivery and breast cell/tissue growth. *Mater Sci Eng C Mater Biol Appl.* 2020;112:110794.
60. Dang HP, et al. Local doxorubicin delivery via 3D-printed porous scaffolds reduces systemic cytotoxicity and breast cancer recurrence in mice. *Adv Therap.* 2020;3(9):2000056.
61. Dehghani S, et al. Multifunctional MIL-Cur@FC as a theranostic agent for magnetic resonance imaging and targeting drug delivery: in vitro and in vivo study. *J Drug Target.* 2020;28(6):668–80.
62. Liu Y, et al. Novel albendazole–chitosan nanoparticles for intestinal absorption enhancement and hepatic targeting improvement in rats. *J Biomed Mater Res.* 2013;101(6):998–1005.
63. Parakh DR, et al. Development and validation of Spectrophotometric method for estimation of mebendazole in bulk and pharmaceutical formulation. *World J Pharm Res.* 2015;4:2223–35.

64. Nejadshafiee V, et al. Magnetic bio-metal–organic framework nanocomposites decorated with folic acid conjugated chitosan as a promising biocompatible targeted theranostic system for cancer treatment. *Mater Sci Eng C*. 2019;99:805–15.
65. Kefayat A, et al. c-phycocyanin: a natural product with radiosensitizing property for enhancement of colon cancer radiation therapy efficacy through inhibition of COX-2 expression. *Sci Rep*. 2019;9(1):1–13.
66. Mukhopadhyay T, et al. Mebendazole elicits a potent antitumor effect on human cancer cell lines both in vitro and in vivo. *J Clin Cancer Res*. 2002;8(9):2963–9.
67. ARAC. Guidelines for endpoints in animal study proposals. Bethesda: Animal Research Advisory Committee; 2011.
68. Workman P, et al. Guidelines for the welfare and use of animals in cancer research. *Br J Cancer*. 2010;102(11):1555–77.
69. Wallace J. Humane endpoints and cancer research. *ILAR J*. 2000;41(2):87–93.
70. Ibrahim KE, et al. Histopathology of the liver, kidney, and spleen of mice exposed to gold nanoparticles. *Molecules*. 2018;23(8):1848.
71. Rajeh MA, et al. Acute toxicity impacts of *Euphorbia hirta* L. extract on behavior, organs body weight index and histopathology of organs of the mice and *Artemia salina*. *Pharmacognosy Res*. 2012;4(3):170–7.
72. Zhang XD, et al. Enhanced tumor accumulation of sub-2 nm gold nanoclusters for cancer radiation therapy. *Adv Healthc Mater*. 2014;3(1):133–41.
73. Beidokhti HRN, et al. Preparation, characterization, and optimization of folic acid-chitosan-methotrexate core-shell nanoparticles by box-behken design for tumor-targeted drug delivery. *AAPS PharmSciTech*. 2017;18(1):115–29.
74. Devendiran RM, et al. Green synthesis of folic acid-conjugated gold nanoparticles with pectin as reducing/stabilizing agent for cancer theranostics. *RSC Adv*. 2016;6(35):29757–68.
75. Esfandiarpour-Boroujeni S, et al. Fabrication and study of curcumin loaded nanoparticles based on folate-chitosan for breast cancer therapy application. *Carbohydr Polym*. 2017;168:14–21.
76. Cheng L, et al. Synthesis of folate-chitosan nanoparticles loaded with ligustrazine to target folate receptor positive cancer cells. *Mol Med Rep*. 2017;16(2):1101–8.
77. Daryasari MP, et al. Chitosan-folate coated mesoporous silica nanoparticles as a smart and pH-sensitive system for curcumin delivery. *RSC Adv*. 2016;6(107):105578–88.
78. Rata-Aguilar A, et al. Colloidal stability and “in vitro” antitumor targeting ability of lipid nanocapsules coated by folate–chitosan conjugates. *J Bioact Compat Polym*. 2012;27(4):388–404.
79. Cao M, et al. Folic acid directly modified low molecular weight of polyethyleneimine for targeted pDNA delivery. *J Drug Deliv Sci Technol*. 2020;56:101522.
80. Gunasekaran S, Uthra D. Vibrational spectra and qualitative analysis of albendazole and mebendazole. *Asian J Chem*. 2008;20(8):6310.
81. Song H, et al. Folic acid-chitosan conjugated nanoparticles for improving tumor-targeted drug delivery. *Biomed Res Int*. 2013;2013:723158.
82. Shen Y, et al. pH-responsive nanoparticles for cancer drug delivery. *Methods Mol Biol*. 2008;437:183–216.
83. Adhikari HS, Yadav PN. Anticancer activity of chitosan, chitosan derivatives, and their mechanism of action. *Int J Biomater*. 2018. <https://doi.org/10.1155/2018/2952085>.
84. Welch DR, Hurst DR. Defining the hallmarks of metastasis. *Cancer Res*. 2019;79(12):3011–27.
85. Kurita K, et al. Enzymatic degradation of  $\beta$ -chitin: susceptibility and the influence of deacetylation. *Carbohydr Polym*. 2000;42(1):19–21.
86. Szymańska E, Winnicka K. Stability of chitosan—a challenge for pharmaceutical and biomedical applications. *Mar Drugs*. 2015;13(4):1819–46.
87. Vårum KM, et al. In vitro degradation rates of partially N-acetylated chitosans in human serum. *Carbohydr Res*. 1997;299(1–2):99–101.
88. Funkhouser JD, Aronson NN Jr. Chitinase family GH18: evolutionary insights from the genomic history of a diverse protein family. *BMC Evol Biol*. 2007;7(1):96.
89. Bekhti A, Piroette J. Hepatotoxicity of mebendazole. Relationship with serum concentrations of the drug. *Gastroenterol Clin Biol*. 1987;11(10):701–3.

## Publisher’s Note

Springer Nature remains neutral with regard to jurisdictional claims in published maps and institutional affiliations.

Ready to submit your research? Choose BMC and benefit from:

- fast, convenient online submission
- thorough peer review by experienced researchers in your field
- rapid publication on acceptance
- support for research data, including large and complex data types
- gold Open Access which fosters wider collaboration and increased citations
- maximum visibility for your research: over 100M website views per year

At BMC, research is always in progress.

Learn more [biomedcentral.com/submissions](https://biomedcentral.com/submissions)

